Compositionally tuned Ni_xSn alloys as anode materials for lithium-ion and sodium-ion batteries with a high pseudocapacitive contribution

Junshan Li,[a,b,○] Xijun Xu,[c,d,○] Zhishan Luo,[a] Chaoqi Zhang,[a] Xiaoting Yu,[a] Yong Zuo,[a] Ting Zhang,[e] Pengyi Tang,[e] Jordi Arbiol,[e,f] Jordi Llorca,[g] Jun Liu,[c,d,*] Andreu Cabot[a,f,*]

a Catalonia Institute for Energy Research - IREC, Sant Adrià de Besòs, Barcelona, 08930, Spain

b Departament d'Electronica, Universitat de Barcelona, 08028 Barcelona, Spain

c Guangdong Provincial Key Laboratory of Advanced Energy Storage Materials, School of Materials Science and Engineering, South China University of Technology, Guangzhou 510641, P. R. China

d SUNWODA-SCUT Joint Laboratory for Advanced Energy Storage Technology, South China University of Technology, Guangzhou 510641, P. R. China

e Catalan Institute of Nanoscience and Nanotechnology (ICN2), CSIC and BIST, Campus UAB, Bellaterra, 08193 Barcelona, Spain

f ICREA, Pg. Lluís Companys 23, 08010 Barcelona, Spain

g Institute of Energy Technologies, Department of Chemical Engineering and Barcelona Research Center in Multiscale Science and Engineering. Universitat Politècnica de Catalunya, EEBE, 08019 Barcelona, Spain

ABSTRACT

Nickel tin alloy nanoparticles (NPs) with tuned composition Ni_xSn ($0.6 \leq x \leq 1.9$) were synthesized by a solution-based procedure and used as anode materials for Li-ion batteries (LIBs) and Na-ion batteries (SIBs). $Ni_{0.9}Sn$-based electrodes exhibited the best performance in both LIBs and SIBs. As LIB anodes, $Ni_{0.9}Sn$-based electrodes delivered charge-discharge capacities of 980 mAh g^{-1} after 340 cycles at 0.2 A g^{-1} rate, which surpassed their maximum theoretical capacity considering that only Sn is lithiated. A kinetic characterization of the charge-discharge process demonstrated the electrode performance to be aided by a significant pseudocapacitive contribution that compensated for the loss of energy storage capacity associated to the solid-electrolyte interphase formation. This significant pseudocapacitive contribution translates in faster kinetics and longer durability and is associated to the small size of the crystal domains and the proper electrode composition. The performance of Ni_xSn-based electrodes toward Na-ion storage was also characterized, reaching moderate capacities above 200 mAh g^{-1} at 0.1 A g^{-1} but with a relatively fast fade over 120 continuous cycles. A relatively larger pseudocapacitive contribution was obtained in Ni_xSn-based electrodes for SIBs, consistently with the lower contribution of the Na ion diffusion.

Keywords: bimetallic nanoparticles; nickel tin alloy; anode materials; lithium-ion batteries; sodium-ion batteries; colloidal nanoparticles

INTRODUCTION

Lithium ion batteries (LIBs) have become essential in a wide range of portable applications. While widely spread in the market, current LIBs are far from being an optimum electrochemical energy storage devices.[1–5] LIBs still suffer from moderate durabilities and current densities in part associated to the employed electrode materials. Additionally, the availability of lithium poses middle-long term limitations to this technology. Thus, the development of improved electrode materials for LIBs and alternative battery technologies based on more abundant ions, such as sodium, is a worthwhile endeavor.

Current commercial LIBs use graphite as anode material, what limits its theoretic maximum energy density to 375 mAh g^{-1}.[6–8] On the other hand, sodium ion batteries (SIBs) cannot make use of graphite due to the insignificant Na-insertion in this material.[9–11] As an alternative anode material, Sn and Sn-based alloys have been extensively studied due to their abundance, low toxicity and high energy density, 992 mAh g^{-1} for LIBs and 847 mAh g^{-1} for SIBs corresponding to the formation of $Li_{22}Sn_5$ and $Na_{15}Sn_4$, respectively.[12–15] However, Sn undergoes huge volume changes during charge-discharge cycles that shorten its usage time.[16–21] This drawback can be partially overcome by reducing the size of the crystal domains in the electrode, which additionally provides advantages in terms of increasing rate capability because of the shorter Li-ion diffusion paths and increasing the pseudocapacitive contribution associated with the larger surface/volume ratios.[22–27] An additional strategy to improve stability is alloying tin with non-active elements, which reduces the volume changes and could also potentially increase the pseudocapacitive contribution. In this direction, Cu-Sn,[28–30] Co-Sn,[31–50] FeSn[30,46] and Ni-Sn[14,30,51–53] alloys among other have been tested as base materials for LIB and/or SIB electrodes with excellent results.

Not considering pseudocapacitive effects, as a drawback of alloying Sn with non-active metals, the maximum energy density potentially achieved decreases with the amount on non-active metal introduced. Thus, the alloy composition needs to be finely tuned to optimize performance. However, most previous works have focused on studding the performance of few particular intermetallic Ni-Sn alloys, with constrained compositions. In the present work, we take advantage of the versatility of colloidal synthesis method to produce nanoparticles (NPs) with controlled crystal phase and composition, to produce NPs of a range of Ni-Sn solid solutions with Ni:Sn ratios from 0.6 to 1.9. After removing surface ligands, we use these NPs to test the performance Ni-Sn solid solutions as anode materials for LIBs and SIBs.

EXPERIMENTAL

Chemicals: Nickel(II) acetylacetonate (Ni(acac)$_2$·xH$_2$O (x~2), 95%, Sigma-Aldrich), tin(II) acetate (Sn(oac)$_2$, 95%, Fluka), oleic acid (OAc, Sigma-Aldrich), oleylamine (OAm, 80-90%, TCI), tri-*n*-octylphosphine (TOP, 97%, Strem), borane tert-butylamine complex (TBAB, 97%, Sigma-Aldrich), TIMCAL Graphite & Carbon Super P (Super P, KJ group), polyvinylidene fluoride (PVDF, KJ group), N-methy1-2-pyrrolidone (NMP, 99%, Aladdin), hydrazine monohydrate (N$_2$H$_4$ 64-65%, reagent grade, 98%, Sigma-Aldrich) and acetonitrile (CH$_3$CN, extra dry, Fisher) were used as received without any further purification. Chloroform, acetone, ethanol, Li-ion and Na-ion electrolyte were of analytical grade and purchased from various sources. An argon-filled glove-box was used for storing and dealing with sensitive chemicals.

Colloidal Synthesis of NiSn NPs: All the syntheses were carried out using standard airless techniques using a vacuum/dry argon gas Schlenk line. Ni-Sn NPs were prepared following a scale-up protocol as the one we previously detailed.[54] Briefly, 20 mL OAm, 1.0 mL OAc, 0.9 mmol Ni(acac)$_2$·xH$_2$O and 0.6 mmol Sn(oac)$_2$ were loaded into a 50 mL three-neck flask containing a magnetic stirring bar. The reaction was strongly stirred and degassed under vacuum at 80 °C for 2 hours to remove water, air, and low-boiling point impurities. Then, a gentle flow of argon was introduced, 5 mL of TOP were injected and the reaction flask was heated to 180 °C at 5 °C/min. Meanwhile, a reducing solution was prepared by dissolving 5 mmol TBAB in 5 mL OAm through sonication for 30 min, and subsequently degassed this mixture for 1 hour at ambient temperature. This reducing solution was injected into the reaction flask containing the Ni and Sn precursor at 180 °C. Upon injection, a visible color change, from deep green to black, was immediately observed. The reaction was maintained at 180 °C for 1 hour, followed by a rapid cool down to room temperature using a water bath. The content of the reaction mixture was transferred to two centrifuge tubes, followed by centrifugation at 9000 rpm for 3 min after introducing acetone as non-solvent. The precipitate was suspended in chloroform and centrifuged again after adding additional acetone. This process was repeated twice. Finally, the NPs were suspended in 10 mL chloroform.

Ligand removal: The native organic ligands were removed from the NP surface according to a previously published report.[25,55] Briefly, 25 mL acetonitrile and 0.8 mL hydrazine hydrate was introduced into a vial containing the precipitated NPs. The mixture was stirred for 4 hours at room temperature and then collected by centrifugation at low speed. The product was further washed with acetonitrile and centrifuged at 2000 rpm for another 3 times. NPs were collected and stored in inert air atmosphere after drying under vacuum at room temperature.

Characterization: Powder x-ray diffraction (XRD) was measured on a Bruker AXS D8 Advance x-ray diffractometer with Cu K radiation (λ = 1.5106 Å) operating at 40 kV and 40 mA. Scanning

electron microscopy (SEM) analyses were performed on a ZEISS Auriga SEM with an energy dispersive X-ray spectroscopy (EDS) detector at 20 kV. Transmission electron microscopy (TEM) analyses were carried out on a ZEISS LIBRA 120, operating at 120 kV, using a 200 mesh Carbon-coated grid from Ted-Pella as substrate. High-resolution TEM (HRTEM) and scanning TEM (STEM) studies were carried out using a field emission gun FEI Tecnai F20 microscope at 200 kV with a point-to-point resolution of 0.19 nm. High angle annular dark-field (HAADF) STEM was combined with electron energy loss spectroscopy (EELS) in the Tecnai microscope by using a GATAN QUANTUM filter. X-ray photoelectron spectroscopy (XPS) was done on a SPECS system equipped with an Al anode XR50 source operating at 150 mW and a Phoibos 150 MCD-9 detector. The pressure in the analysis chamber was kept below 10^{-7} Pa. The area analyzed was about 2 mm x 2 mm. The pass energy of the hemispherical analyzer was set at 25 eV and the energy step was maintained at 1.0 eV. Data processing was performed with the Casa XPS program (Casa Software Ltd., UK). Binding energies were shifted according to the reference C 1s peak that was located at 284.8 eV. The Fourier transform infrared spectrometer (FTIR) data were recorded on an Alpha Bruker spectrometer.

Electrochemical measurements: Ni-Sn NPs (80 wt%) were mixed with Super P (10 wt%), polyvinylidene fluoride (PVDF, 10 wt%) and N-methyl-2-pyrrolidone (NMP). The obtained slurry was bladed onto a coper foil and dried at 80 ℃ for 24 h in a vacuum oven. Working electrodes were obtained by cutting the printed foil into circular disk with a diameter of 12.0 mm. The mass loading of active materials was estimated to be 0.7-1.2 mg cm^{-2}. To test the performance of electrodes based on Ni-Sn NPs, half cells were assembled in the glove box (H$_2$O and O$_2$ < 0.1 ppm) using Celgard2400 as separator. As electrolyte for LIBs, a 1 M LiPF$_6$ solution in ethylene carbonate (EC)/diethyl carbonate (DEC) (1:1 in volume) with 5 vol% fluoroethylene carbonate (FEC) as additive was used. For SIBs, 1 M NaClO$_4$ in propylene carbonate (PC)/ EC (1:1 in volume) with 5 vol% FEC was used as the electrolyte. Galvanostatic charge-discharge were measured by a battery test system (CT2001A, LAND) with cutoff potentials from 0.01 V to 3.0 V. Cyclic voltammograms (CV) were obtained using an electrochemical workstation (Gamry Interface 1000) in the voltage range from 0–3.0 V at scan rates from 0.1 mV s^{-1} to 1 mV s^{-1}.

RESULTS AND DISCUSSION

Ni_xSn NPs with tuned composition ($0.6<x<1.9$) were prepared by the co-reduction of proper amounts of nickel(II) acetylacetonate and tin(II) acetate at 180 ℃ by TBAB and in the presence of OAm and OAc (see experimental section for details). Following this procedure, quasi-spherical NPs with sizes in the range from 3.9 ± 0.7 nm to 4.6 ± 0.6 nm were produced (Figure 1). SEM-EDS analysis showed the Ni/Sn ratio of the Ni_xSn NPs to be 0.6, 0.9, 1.2 and 1.9 ± 0.1 for nominal Ni/Sn ratios of 0.75, 1.0, 1.5 and 2.0, respectively (Figure S1). XRD analysis displayed the crystallographic phase of all the alloys to resemble that of Sn or orthorhombic Ni_3Sn_2. Main XRD peaks did not significantly shift with the introduction of different amounts of Ni due to their relatively similar atomic radius. However, as the Ni amount increased, the material crystallinity decreased and additional peaks became visible, denoting the formation of a more complex crystal phase, which did not match well with any of the reported intermetallic Ni-Sn phases.
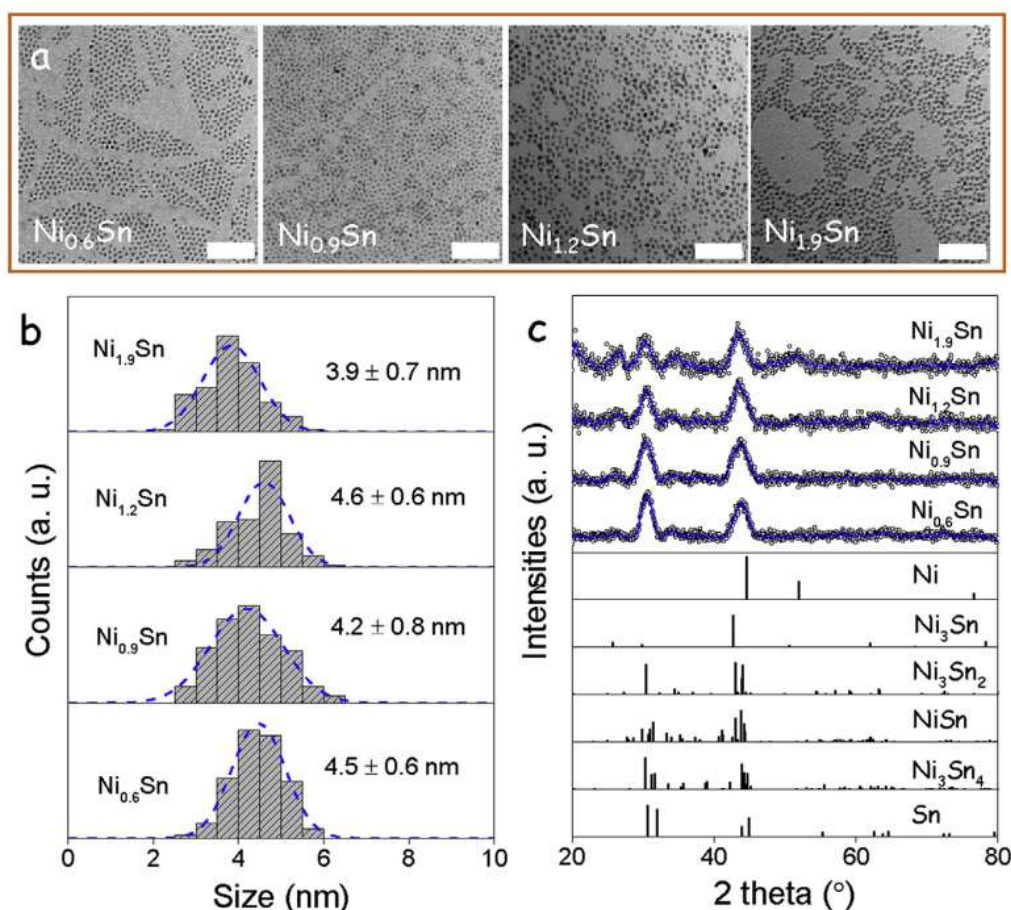

Figure 1. a) TEM micrographs of Ni-Sn NPs with different compositions, as obtained from EDX and displayed in each image. Scale bar: 50 nm. b) Size distribution histograms of the Ni-Sn NPs; c) XRD patterns of the NPs with different compositions. Sn, Ni and different Ni-Sn intermetallic XRD patterns are shown as reference.

EELS chemical composition maps showed Ni and Sn to be present in all the NPs with similar ratio. Additionally, uniform distributions of Ni and Sn within each NP were observed (Figure 2a). HRTEM analysis revealed the NPs to have a good crystallinity with a crystallographic phase in agreement with Ni or the Ni_3Sn_2 orthorhombic phase (space group = Pnma) with a = 7.1100 Å, b = 5.2100 Å and c = 8.2300 Å (Figure 2b). [56]
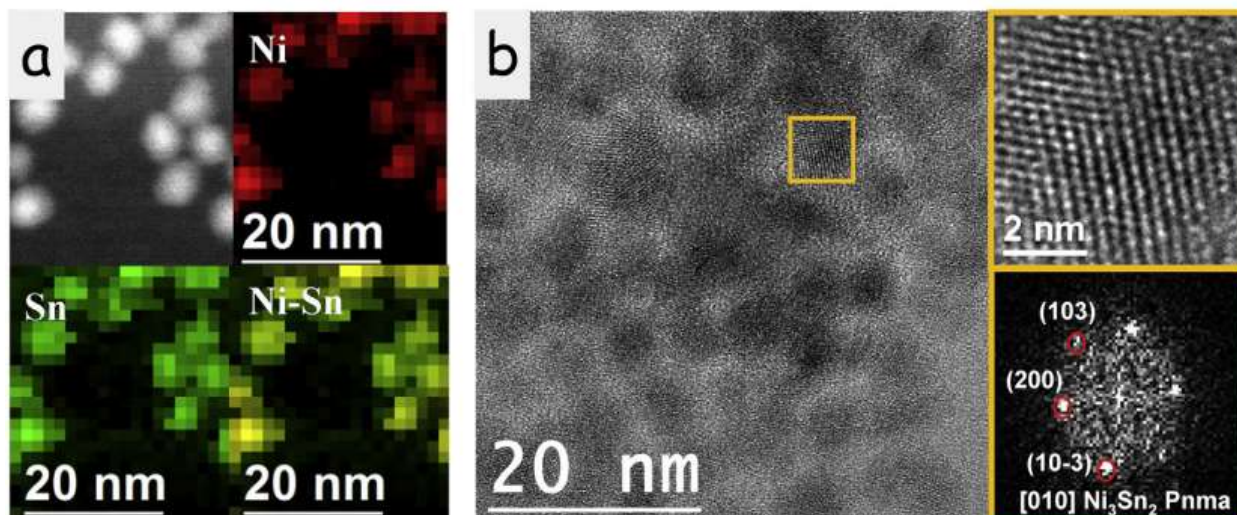
Figure 2. a) STEM and EELS compositional maps of $Ni_{0.6}Sn$ NPs. b) HRTEM micrograph of $Ni_{0.6}Sn$ NPs exposed to atmosphere and displaying a core-shell type structure. The Ni_3Sn_2 lattice fringe distances were measured to be 0.260 nm, 0.337 nm and 0.269 nm, at 69.40 and 134.54° which could be interpreted as the orthorhombic Ni_3Sn_2 phase, visualized along its [010] zone axis

As displayed in Figures 3 and S2, XPS analysis of the Ni_xSn NPs showed Ni to be present in two different chemical states, which we associated with metallic Ni^0 (Ni $2p_{3/2}$ at 852.3 eV) and $Ni^{2+/3+}$ oxidation states (Ni $2p_{3/2}$ at 855.6 eV).[57] The ratio of the two components was found to be $Ni^{2+/3+}/Ni^0$ = 2.5. Sn was also present in two chemical states, displaying a metallic (Sn $3d_{5/2}$ peak at 484.4 eV) and an oxidized component (Sn $3d_{5/2}$ peak at 486.2 eV) with a relative ratio $Sn^{2+/4+}/Sn^0$ = 3.2.[57] We associated the oxidized states to the presence of an oxide layer at the Ni_xSn NPs surface grown during their manipulation and transportation in ambient conditions. The ratio of the two metals measured by XPS in the $Ni_{1.2}Sn$ NPs was Ni/Sn = 0.46, which pointed at a slight segregation of Sn to the NP surface, also consistent with the higher relative oxidized component in Sn than Ni. We hypothesize that this surface segregation could have taken place during oxidation.[54,58,59]
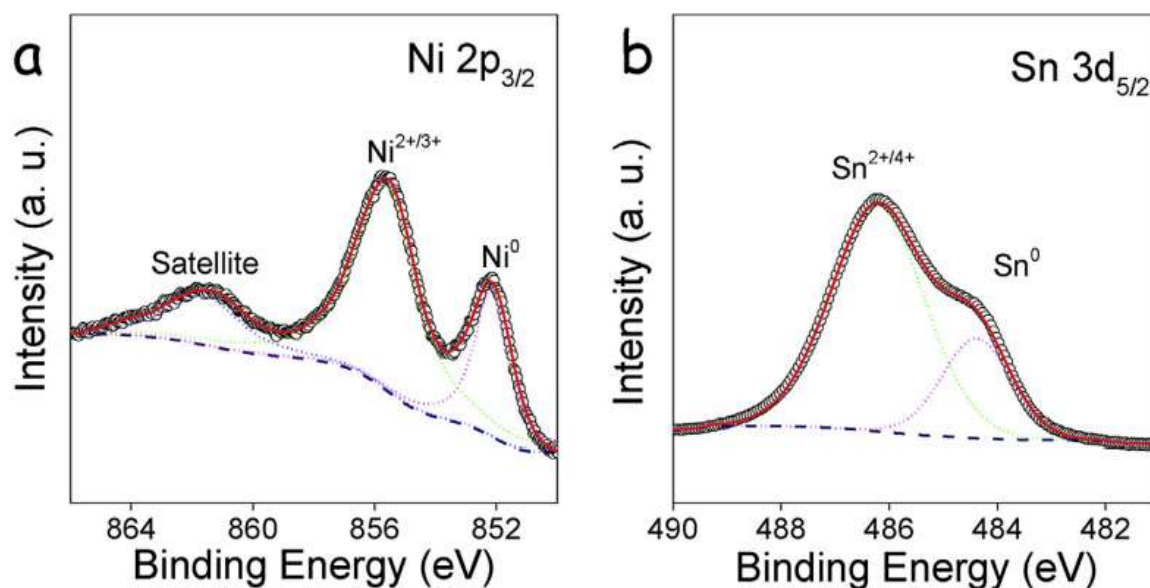
6

Figure 3. XPS spectra of the Ni $2P_{3/2}$ region (a) and of the Sn $3d_{5/2}$ region (b) of $Ni_{1.2}Sn$ NPs.

Before testing the performance of Ni_xSn NPs as anode material in LIBs and SIBs, the organic ligands present at their surface were removed though a treatment with a mixture of hydrazine and acetonitrile. FTIR analysis confirmed the effectivity of this treatment through the disappearance of peaks at 2890 cm^{-1} and 2822 cm^{-1} that correspond to C-H stretching modes (Figure S3).

To test the performance of Ni_xSn NPs as anode material in LIBs and SIBs, coin-type half-cells with metallic Li or Na as counter electrodes were used. Working electrodes were prepared by mixing Ni_xSn NPs with Super P, PVDF and NMP and coating the resulting slurry onto Cu foil. Standard liquid electrolyte formulations were used: $LiPF_6$ in EC/DEC with FEC for LIBs and $NaClO_4$ in PC/EC with FEC for SIBs.

Figure 4 shows representative initial CVs of the $Ni_{0.9}Sn$ NP-based electrode obtained at 0.1 mV s^{-1} in the applied potential 0-3.0 V vs. Li^+/Li and Na^+/Na, respectively. Significant differences were obtained between the 1st and following cycles, associated to the formation of the SEI layer in both systems.[14]
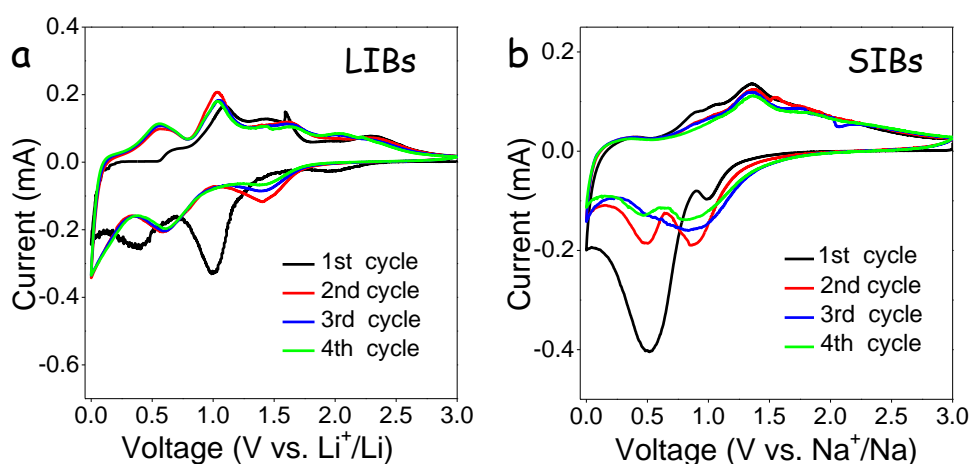
Figure 4. Initial CVs obtained from the $Ni_{0.9}Sn$ NP-based electrode at 0.1 mV s^{-1} in the voltage window 0-3.0 V *vs.* (a) Li^+/Li (b) Na^+/Na.

Lithium is reversibly intercalated within Sn with a theoretical capacity of 992 mAh g^{-1} corresponding to the conversion reaction: $Sn \rightarrow Li_{4.4}Sn$.[43] Lithium does not intercalate in Ni. Thus, assuming no contribution from Ni, the theoretical capacity of $Ni_{0.6}Sn$, $Ni_{0.9}Sn$, $Ni_{1.2}Sn$ and $Ni_{1.9}Sn$ electrodes was 765 mAh g^{-1}, 687 mAh g^{-1}, 623 mAh g^{-1}, and 511 mAh g^{-1}, respectively.

The capacity of Ni_xSn NP-based electrodes when cycled at 0.2 A g^{-1} is shown in Figures 4 and S4. Ni_xSn NP-based electrodes delivered very large initial capacities, well above their theoretical maximum, with values up to 1200 mAh g^{-1} for all electrodes. However, in the first very few cycles, a very strong loss in the current density was observed due to the SEI layer formation. Upon continuous cycling, the charge-discharge capability decreased during the first 70 cycles, but recovered after some additional cycles up to values well above their theoretical maximum capacity, e.g. 980 mAh g^{-1} after 340 cycles for the $Ni_{0.9}Sn$ electrode (Figure 4b). On the other hand, the columbic efficiency was stabilized at ca. 99% after the first 10 cycles. Among the different Ni_xSn compositions, $Ni_{0.9}Sn$ showed the highest cycling performance (Figure S4).
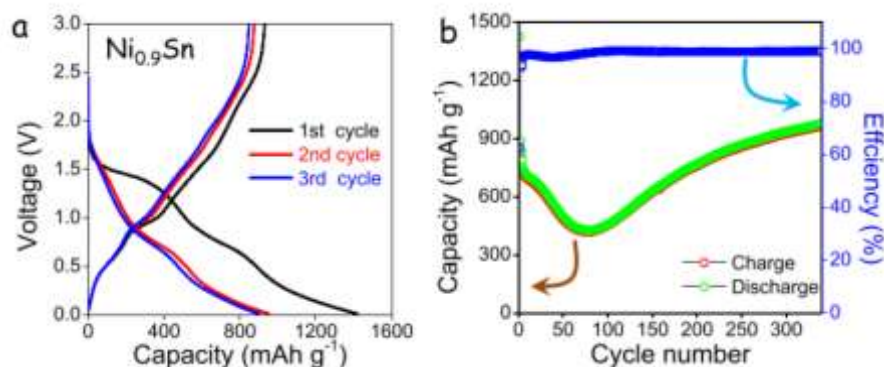

Figure 4. a) Initial charge-discharge curves at 0.2 A g^{-1} for the $Ni_{0.9}Sn$ electrode. b) Charge-discharge capacity and related efficiency over 340 cycles at a current density of 0.2 A g^{-1}.

To further evaluate the rate capability of the $Ni_{0.9}Sn$ NP-based electrodes, galvanostatic measurements were carried out at different current densities, between 0.1 and 2.0 A g^{-1} (Figure 5). $Ni_{0.9}Sn$ NP-based electrodes delivered average discharge capacities of 835, 702, 523, 378 and 261 mAh g^{-1} at 0.1, 0.2, 0.5, 1.0, 2.0 A g^{-1}, respectively.
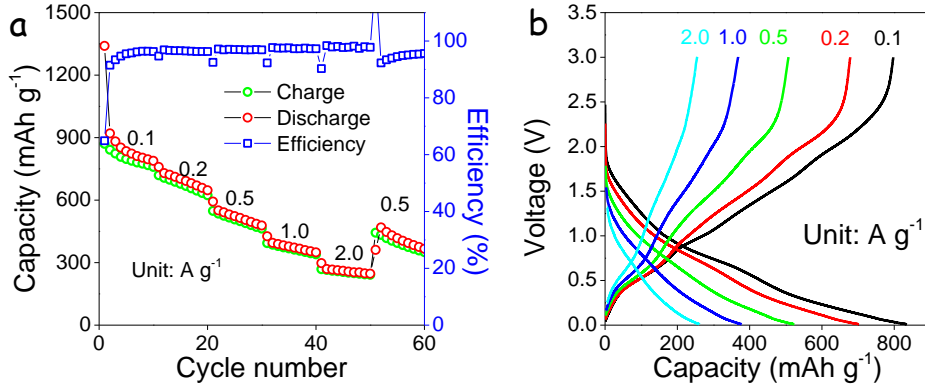

Figure 5. Li-ion storage performance of the $Ni_{0.9}Sn$ electrode: a) Charge-discharge curves at rates: 0.1, 0.2, 0.5, 1.0, 2.0, 0.5 A g^{-1}. b) Rate performance at 0.1, 0.2, 0.5, 1.0, 2.0 A g^{-1}.

The kinetics of $Ni_{0.9}Sn$ NP-based electrodes in LIBs was investigated by collecting CVs at different scan rates: 0.1, 0.2, 0.4, 0.7, 1.0 mV s^{-1} in the potential range 0-3.0 V vs. Li$^+$/Li (Figure 6a). Three anodic peaks, at 0.62, 0.54 and 1.04 V were observed to increase with scan rate. Generally, a relationship between the measured current (i) and the scan rate (v) can be considered: [60–62]

$$i = av^b$$

According to previous reports, a diffusion controlled process is characterized by b = 0.5. On the other hand, an ideal capacitive behavior is indicated by b = 1.[54–57] From our experimental results, the b values of the current peaks at 0.62, 0.54, 1.04 V were calculated to be 0.83, 0.66 and 0.63, respectively. b values above b = 0.5 indicated a relatively fast kinetics resulting from a pseudocapacitive effect (Figure 6b).

At a given potential, the current density at each scan rate can be divided into two contributions, a diffusion-controlled ($k_1v^{1/2}$) associated to the Li$^+$ insertion and a capacitor-like fraction (k_2v): [54–57]

$$i(V) = k_1v^{1/2} + k_2v$$

Thus, k_1 and k_2 can be determined by plotting $i(V)/v^{1/2}$ vs. $v^{1/2}$, distinguishing in this way the two contributions. Figure 6c shows a CV at 0.4 mV s^{-1} where the two components have been differentiated: the capacitive current as the blue shaded region and the diffusion component in red. Similarly, the two contributions are differentiated in the CVs at 0.1, 0.2, 0.7 and 1.0 mV s^{-1} in Figure S5. All these data are summarized in Figure 6d. Overall, increasing capacitive contributions were

obtained when increasing the scan rate and a capacitive contribution up to 72% was reached at 1.0 mV s^{-1}. Such relatively high capacitive contributions are highly beneficial because it is a much faster and stable process than the diffusion-controlled alloying and at the same time it is generally associated with improved stability.
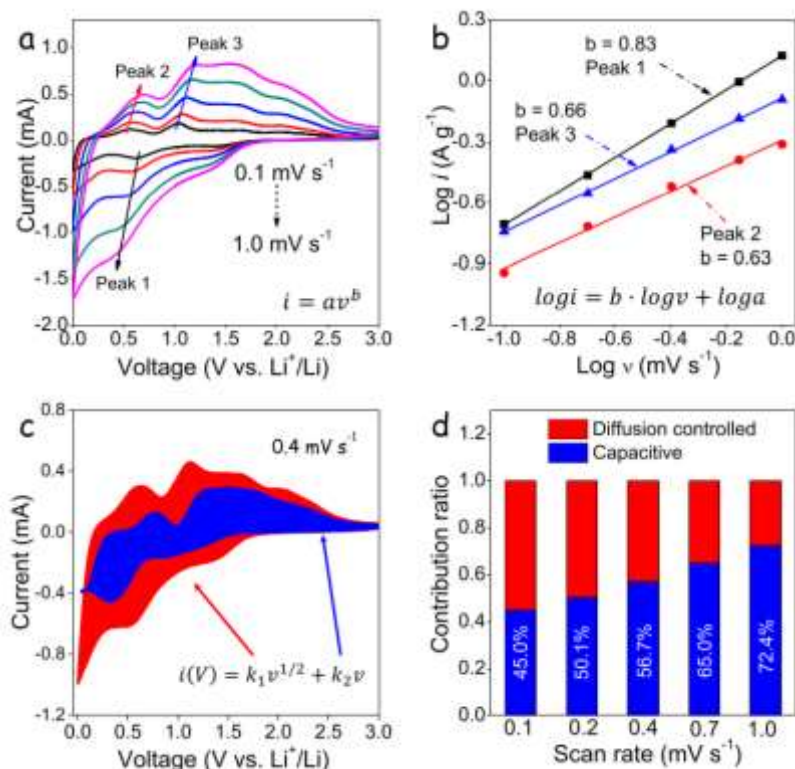

Figure 6. Li-ion storage performance of the $Ni_{0.9}Sn$ electrode: a) CV curve at the scan rates of 0.1, 0.2, 0.4, 0.7, 1.0 mV s^{-1}. b) Logarithmic dependence between peak current density and scan rate at the anodic peaks 0.62, 0.54, 1.04V. c) Capacitive contribution to the total current contribution at 0.4 mV s^{-1}. d) Normalize capacitive and diffusion-controlled contribution at the scan rates of 0.1, 0.2, 0.4, 0.7, 1.0 mV s^{-1}.

Sodium is also reversibly stored in Sn, with a maximum theoretical capacity of 847 mAh g^{-1} corresponding to the reaction: $Sn \rightarrow Na_{3.75}Sn$.[14] Considering that Ni does not contribute to any Na-ion capacity, thus the theoretical capacity of $Ni_{0.6}Sn$, $Ni_{0.9}Sn$, $Ni_{1.2}Sn$ and $Ni_{1.9}Sn$ electrodes is 653 mAh g^{-1}, 586 mAh g^{-1}, 532 mAh g^{-1}, and 437 mAh g^{-1}, respectively.

Figures 7 and S6 present the Na-ion storage performance of Ni_xSn NP-based electrodes over 120 cycles at 0.1 A g^{-1}. Again, among the different compositions tested, $Ni_{0.9}Sn$ NPs exhibited the best performance. In the first cycles, Na-ion discharge-charge storage capacities above 300 mAh g^{-1} at 0.1 A g^{-1} were obtained for the $Ni_{0.9}Sn$ NP-based electrode. However, upon subsequent cycling, a monotonous capacity decrease was observed, down to 160 mAh g^{-1} at the 120th cycle. Rate-capability tests in the window 0.1-2.0 A g^{-1} showed the $Ni_{0.9}Sn$ NP-based electrode to deliver average discharge

capacities of 327, 258, 217, 168, 128, and 88 mAh g⁻¹ at 0.05, 0.1, 0.2, 0.5, 1.0, and 2.0 A g⁻¹, respectively. In addition, $Ni_{0.9}Sn$ NP-based electrodes showed similar capacities at 0.1 and 0.2 A g⁻¹ after 30-40 more cycles at higher charging rate.
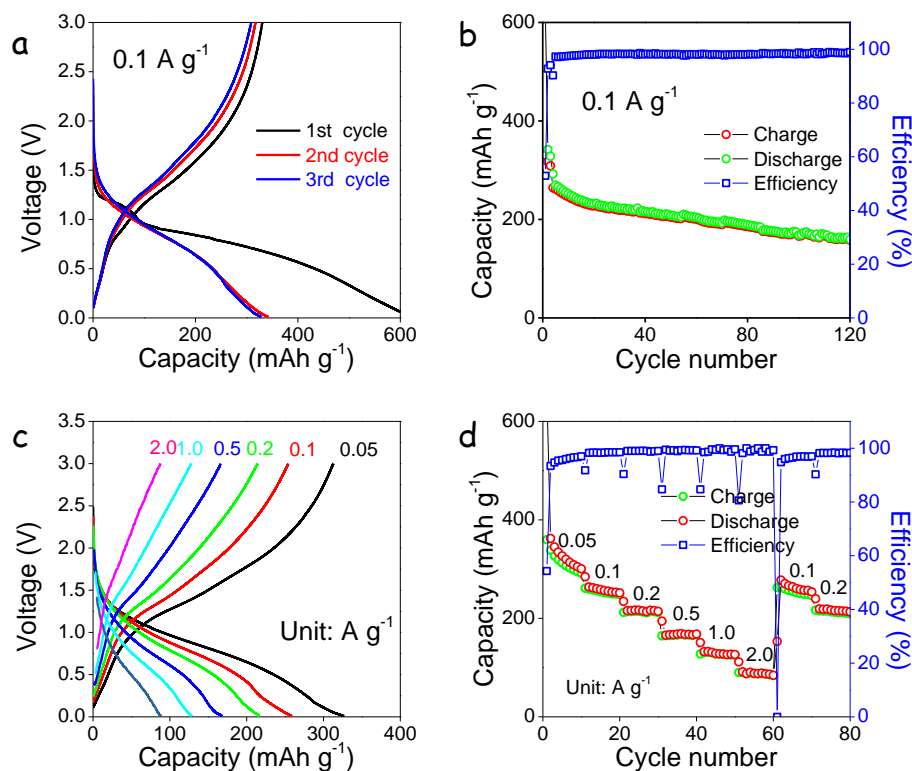

Figure 7. Na-ion storage performance of the $Ni_{0.9}Sn$ electrode: a) Initial charge-discharge curves at 0.1 A g⁻¹. b) Charge-discharge capacity and related efficiency over 120 cycles at a current density of 0.1 A g⁻¹. c) Charge-discharge curves at rates: 0.05, 0.1, 0.2, 0.5, 1.0, 2.0, 0.1 and 0.2 A g⁻¹. d) Rate performance at 0.05, 0.1, 0.2, 0.5, 1.0 and 2.0 A g⁻¹.

The kinetics of $Ni_{0.9}Sn$ NP-based electrodes in SIBs was investigated in a similar way as in LIBs, by collecting CVs at different scan rates: 0.1, 0.2, 0.4, 0.7, 1.0 mV s⁻¹. $Ni_{0.9}Sn$ NP-based electrodes in SIBs were characterized with b values of 0.91 and 0.84 at 0.85 V and 1.36 V, respectively. Higher b values already pointed out at a relatively higher capacitance contribution in SIBs than LIBs. As shown in Figure S7, contributions up to 84% at 1.0 mV s⁻¹ were measured from $Ni_{0.9}Sn$ NP-based electrodes in SIBs.

CONCLUSION

In summary, we report the synthesis of Ni_xSn NPs with tuned composition (0.6≤ x ≤1.9) and their performance as anode material in LIBs and SIBs. Among the different compositions tested, best performances toward Li⁺ ion and Na⁺ ion insertion were obtained for $Ni_{0.9}Sn$ NP-based electrodes. This optimized cycling charge-discharge performance for LIBs provided 980 mAh g⁻¹ at 0.2 A g⁻¹ after

340 cycles. Additionally, $Ni_{0.9}Sn$ NP-based electrodes were tested in Na^+-ion half cells, exhibiting 160 mAh g^{-1} over 120 cycles at 0.1 A g^{-1}. From CV measurements at different current rates, it was found that the charging process was both capacitive and diffusion controlled, while the capacitive contribution was dominant in both LIBs and SIBs. The pseudocapacitive charge-storage accounted for a high portion of the whole energy storage capacity, which was associated to the small size and composition of the Ni_xSn NPs used.

Conflict of interest

The authors declare no competing financial interest.

Supporting Information

Supplementary material related to this article can be found.

References

(1)   Park, C.-M.; Kim, J.-H.; Kim, H.; Sohn, H.-J. Li-Alloy Based Anode Materials for Li Secondary Batteries. *Chem. Soc. Rev.* **2010**, *39* (8), 3115.

(2)   Larcher, D.; Tarascon, J.-M. Towards Greener and More Sustainable Batteries for Electrical Energy Storage. *Nat. Chem.* **2015**, *7* (1), 19–29.

(3)   Goodenough, J. B.; Park, K.-S. The Li-Ion Rechargeable Battery: A Perspective. *J. Am. Chem.*

Soc. **2013**, *135* (4), 1167–1176.

(4)   Slater, M. D.; Kim, D.; Lee, E.; Johnson, C. S. Sodium-Ion Batteries. *Adv. Funct. Mater.* **2013**, *23* (8), 947–958.

(5)   Palacín, M. R. Recent Advances in Rechargeable Battery Materials: A Chemist's Perspective. *Chem. Soc. Rev.* **2009**, *38* (9), 2565.

(6)   Wen, Y.; He, K.; Zhu, Y.; Han, F.; Xu, Y.; Matsuda, I.; Ishii, Y.; Cumings, J.; Wang, C. Expanded Graphite as Superior Anode for Sodium-Ion Batteries. *Nat. Commun.* **2014**, *5*, 4033.

(7)   Oszajca, M. F.; Bodnarchuk, M. I.; Kovalenko, M. V. Precisely Engineered Colloidal Nanoparticles and Nanocrystals for Li-Ion and Na-Ion Batteries: Model Systems or Practical Solutions? *Chem. Mater.* **2014**, *26* (19), 5422–5432.

(8)   Liu, N.; Lu, Z.; Zhao, J.; McDowell, M. T.; Lee, H.-W.; Zhao, W.; Cui, Y. A Pomegranate-Inspired Nanoscale Design for Large-Volume-Change Lithium Battery Anodes. *Nat. Nanotechnol.* **2014**, *9* (3), 187–192.

(9)   Nacimiento, F.; Lavela, P.; Tirado, J. L.; Jiménez-Mateos, J. M. A Facile Carbothermal Preparation of Sn–Co–C Composite Electrodes for Li-Ion Batteries Using Low-Cost Carbons. *J. Solid State Electrochem.* **2012**, *16* (3), 953–962.

(10)   Hwang, J.-Y.; Myung, S.-T.; Sun, Y.-K. Sodium-Ion Batteries: Present and Future. *Chem. Soc. Rev.* **2017**, *46* (12), 3529–3614.

(11)   Lao, M.; Zhang, Y.; Luo, W.; Yan, Q.; Sun, W.; Dou, S. X. Alloy-Based Anode Materials toward Advanced Sodium-Ion Batteries. *Adv. Mater.* **2017**, *29* (48).

(12)   Bruce, P. G.; Scrosati, B.; Tarascon, J.-M. Nanomaterials for Rechargeable Lithium Batteries. *Angew. Chemie Int. Ed.* **2008**, *47* (16), 2930–2946.

(13)   Tian, H.; Xin, F.; Wang, X.; He, W.; Han, W. High Capacity Group-IV Elements (Si, Ge, Sn) Based Anodes for Lithium-Ion Batteries. *J. Mater.* **2015**, *1* (3), 153–169.

(14)   Liu, J.; Wen, Y.; van Aken, P. A.; Maier, J.; Yu, Y. Facile Synthesis of Highly Porous Ni–Sn Intermetallic Microcages with Excellent Electrochemical Performance for Lithium and Sodium Storage. *Nano Lett.* **2014**, *14* (11), 6387–6392.

(15)   Marom, R.; Amalraj, S. F.; Leifer, N.; Jacob, D.; Aurbach, D. A Review of Advanced and Practical Lithium Battery Materials. *J. Mater. Chem.* **2011**, *21* (27), 9938–9954.

(16)   Wen, J.; Yu, Y.; Chen, C. A Review on Lithium-Ion Batteries Safety Issues: Existing Problems and Possible Solutions. *Mater. Express* **2012**, *2* (3), 197–212.

(17)   Wang, B.; Luo, B.; Li, X.; Zhi, L. The Dimensionality of Sn Anodes in Li-Ion Batteries. *Mater. Today* **2012**, *15* (12), 544–552.

(18)   Vaalma, C.; Buchholz, D.; Weil, M.; Passerini, S. A Cost and Resource Analysis of Sodium-Ion Batteries. *Nat. Rev. Mater.* **2018**, *3* (4), 18013.

(19)   Obrovac, M. N.; Chevrier, V. L. Alloy Negative Electrodes for Li-Ion Batteries. *Chem. Rev.* **2014**, *114* (23), 11444–11502.

(20)   Nitta, N.; Wu, F.; Lee, J. T.; Yushin, G. Li-Ion Battery Materials: Present and Future. *Mater. Today* **2015**, *18* (5), 252–264.

(21)   Kamali, A. R.; Fray, D. J. Tin-Based Materials as Advanced Anode Materials for Lithium Ion Batteries: A Review. *Rev. Adv. Mater. Sci.* **2011**, *27* (1), 14–24.

(22)   Walter, M.; Doswald, S.; Krumeich, F.; He, M.; Widmer, R.; Stadie, N. P.; Kovalenko, M. V. Oxidized Co–Sn Nanoparticles as Long-Lasting Anode Materials for Lithium-Ion Batteries. *Nanoscale* **2018**, *10* (8), 3777–3783.

(23)   Oszajca, M. F.; Bodnarchuk, M. I.; Kovalenko, M. V. Precisely Engineered Colloidal Nanoparticles and Nanocrystals for Li-Ion and Na-Ion Batteries: Model Systems or Practical Solutions? *Chem. Mater.* **2014**, *26* (19), 5422–5432.

(24)   Kravchyk, K.; Protesescu, L.; Bodnarchuk, M. I.; Krumeich, F.; Yarema, M.; Walter, M.; Guntlin, C.; Kovalenko, M. V. Monodisperse and Inorganically Capped Sn and Sn/SnO_2 Nanocrystals for High-Performance Li-Ion Battery Anodes. *J. Am. Chem. Soc.* **2013**, *135* (11), 4199–4202.

(25)   He, M.; Walter, M.; Kravchyk, K. V.; Erni, R.; Widmer, R.; Kovalenko, M. V. Monodisperse SnSb Nanocrystals for Li-Ion and Na-Ion Battery Anodes: Synergy and Dissonance between Sn and Sb. *Nanoscale* **2015**, *7* (2), 455–459.

(26)   Chen, C.; Wen, Y.; Hu, X.; Ji, X.; Yan, M.; Mai, L.; Hu, P.; Shan, B.; Huang, Y. Na^+ Intercalation Pseudocapacitance in Graphene-Coupled Titanium Oxide Enabling Ultra-Fast Sodium Storage and Long-Term Cycling. *Nat. Commun.* **2015**, *6* (1), 6929.

(27)   Brezesinski, T.; Wang, J.; Tolbert, S. H.; Dunn, B. Ordered Mesoporous α-MoO3 with Iso-Oriented Nanocrystalline Walls for Thin-Film Pseudocapacitors. *Nat. Mater.* **2010**, *9* (2), 146–151.

(28)   Lei, W. X.; Pan, Y.; Zhou, Y. C.; Zhou, W.; Peng, M. L.; Ma, Z. S. CNTs–Cu Composite Layer Enhanced Sn–Cu Alloy as High Performance Anode Materials for Lithium-Ion Batteries. *RSC Adv.* **2014**, *4* (7), 3233–3237.

(29)   Lin, Y.-M.; Abel, P. R.; Gupta, A.; Goodenough, J. B.; Heller, A.; Mullins, C. B. Sn–Cu
          Nanocomposite Anodes for Rechargeable Sodium-Ion Batteries. *ACS Appl. Mater. Interfaces*
          2013, *5* (17), 8273–8277.

(30)   Wang, X.-L.; Han, W.-Q.; Chen, J.; Graetz, J. Single-Crystal Intermetallic M−Sn (M = Fe, Cu,
          Co, Ni) Nanospheres as Negative Electrodes for Lithium-Ion Batteries. *ACS Appl. Mater.
          Interfaces* **2010**, *2* (5), 1548–1551.

(31)   Jang, B.-O.; Park, S.-H.; Lee, W.-J. Electrospun Co–Sn Alloy/Carbon Nanofibers Composite
          Anode for Lithium Ion Batteries. *J. Alloys Compd.* **2013**, *574*, 325–330.

(32)   Liu, X.; Xie, J.; Zhao, H.; Lv, P.; Wang, K.; Feng, Z.; Świerczek, K. Electrochemical
          Properties of Mechanochemically Synthesized CoSn2-C Nanocomposite-Type Anode Material
          for Li-Ion Batteries. *Solid State Ionics* **2015**, *269*, 86–92.

(33)   González, J. R.; Nacimiento, F.; Alcántara, R.; Ortiz, G. F.; Tirado, J. L. Electrodeposited
          CoSn2 on Nickel Open-Cell Foam: Advancing towards High Power Lithium Ion and Sodium
          Ion Batteries. *CrystEngComm* **2013**, *15* (44), 9196.

(34)   Gnanamuthu, R.; Jo, Y. N.; Lee, C. W. Brush Electroplated CoSn2 Alloy Film for Application
          in Lithium-Ion Batteries. *J. Alloys Compd.* **2013**, *564*, 95–99.

(35)   Ferrara, G.; Arbizzani, C.; Damen, L.; Guidotti, M.; Lazzari, M.; Vergottini, F. G.; Inguanta,
          R.; Piazza, S.; Sunseri, C.; Mastragostino, M. High-Performing Sn–Co Nanowire Electrodes as
          Anodes for Lithium-Ion Batteries. *J. Power Sources* **2012**, *211*, 103–107.

(36)   Ferguson, P. P.; Todd, A. D. W.; Dahn, J. R. Comparison of Mechanically Alloyed and
          Sputtered Tin–cobalt–carbon as an Anode Material for Lithium-Ion Batteries. *Electrochem.
          commun.* **2008**, *10* (1), 25–31.

(37)   He, J.; Zhao, H.; Wang, J.; Wang, J.; Chen, J. Hydrothermal Synthesis and Electrochemical
          Properties of Nano-Sized Co–Sn Alloy Anodes for Lithium Ion Batteries. *J. Alloys Compd.*
          2010, *508* (2), 629–635.

(38)   Lee, S.-I.; Yoon, S.; Park, C.-M.; Lee, J.-M.; Kim, H.; Im, D.; Doo, S.-G.; Sohn, H.-J. Reaction
          Mechanism and Electrochemical Characterization of a Sn–Co–C Composite Anode for Li-Ion
          Batteries. *Electrochim. Acta* **2008**, *54* (2), 364–369.

(39)   Chen, P.; Guo, L.; Wang, Y. Graphene Wrapped SnCo Nanoparticles for High-Capacity
          Lithium Ion Storage. *J. Power Sources* **2013**, *222*, 526–532.

(40)   Shin, J.; Ryu, W.-H.; Park, K.-S.; Kim, I.-D. Morphological Evolution of Carbon Nanofibers
          Encapsulating SnCo Alloys and Its Effect on Growth of the Solid Electrolyte Interphase Layer.

ACS Nano **2013**, *7* (8), 7330–7341.

(41)   Zhang, J.; Xia, Y. Co-Sn Alloys as Negative Electrode Materials for Rechargeable Lithium Batteries. *J. Electrochem. Soc.* **2006**, *153* (8), A1466.

(42)   Mahmood, N.; Zhang, C.; Liu, F.; Zhu, J.; Hou, Y. Hybrid of Co_3Sn_2 @Co Nanoparticles and Nitrogen-Doped Graphene as a Lithium Ion Battery Anode. *ACS Nano* **2013**, *7* (11), 10307–10318.

(43)   Wang, S.; He, M.; Walter, M.; Krumeich, F.; Kravchyk, K. V.; Kovalenko, M. V. Monodisperse $CoSn_2$ and $FeSn_2$ Nanocrystals as High-Performance Anode Materials for Lithium-Ion Batteries. *Nanoscale* **2018**, *10* (15), 6827–6831.

(44)   Tamura, N.; Kato, Y.; Mikami, A.; Kamino, M.; Matsuta, S.; Fujitani, S. Study on Sn–Co Alloy Anodes for Lithium Secondary Batteries. *J. Electrochem. Soc.* **2006**, *153* (8), A1626.

(45)   Du, Z.; Zhang, S. Enhanced Electrochemical Performance of Sn–Co Nanoarchitectured Electrode for Lithium Ion Batteries. *J. Phys. Chem. C* **2011**, *115* (47), 23603–23609.

(46)   Vogt, L. O.; Villevieille, C. Elucidation of the Reaction Mechanisms of Isostructural $FeSn_2$ and $CoSn_2$ Negative Electrodes for Na-Ion Batteries. *J. Mater. Chem. A* **2017**, *5* (8), 3865–3874.

(47)   Ionica-Bousquet, C. M.; Lippens, P. E.; Aldon, L.; Olivier-Fourcade, J.; Jumas, J. C. In Situ 119 Sn Mössbauer Effect Study of Li−$CoSn_2$ Electrochemical System. *Chem. Mater.* **2006**, *18* (26), 6442–6447.

(48)   Zhu, J.; Wang, D.; Liu, T.; Guo, C. Preparation of Sn-Co-Graphene Composites with Superior Lithium Storage Capability. *Electrochim. Acta* **2014**, *125*, 347–353.

(49)   Shi, X.; Song, H.; Li, A.; Chen, X.; Zhou, J.; Ma, Z. Sn–Co Nanoalloys Embedded in Porous N-Doped Carbon Microboxes as a Stable Anode Material for Lithium-Ion Batteries. *J. Mater. Chem. A* **2017**, *5* (12), 5873–5879.

(50)   Park, G. O.; Yoon, J.; Shon, J. K.; Choi, Y. S.; Won, J. G.; Park, S. Bin; Kim, K. H.; Kim, H.; Yoon, W.-S.; Kim, J. M. Discovering a Dual-Buffer Effect for Lithium Storage: Durable Nanostructured Ordered Mesoporous Co-Sn Intermetallic Electrodes. *Adv. Funct. Mater.* **2016**, *26* (17), 2800–2808.

(51)   ZHANG, D.; YANG, C.; DAI, J.; WEN, J.; WANG, L.; CHEN, C. Fabrication of Sn-Ni Alloy Film Anode for Li-Ion Batteries by Electrochemical Deposition. *Trans. Nonferrous Met. Soc. China* **2009**, *19* (6), 1489–1493.

(52)   Uysal, M.; Cetinkaya, T.; Alp, A.; Akbulut, H. Active and Inactive Buffering Effect on the Electrochemical Behavior of Sn-Ni/MWCNT Composite Anodes Prepared by Pulse Electrodeposition for Lithium-Ion Batteries. *J. Alloys Compd.* **2015**, *645*, 235–242.

(53)   Fan, X.; Dou, P.; Jiang, A.; Ma, D.; Xu, X. One-Step Electrochemical Growth of a Three-Dimensional Sn–Ni@PEO Nanotube Array as a High Performance Lithium-Ion Battery Anode. *ACS Appl. Mater. Interfaces* **2014**, *6* (24), 22282–22288.

(54)   Li, J.; Luo, Z.; Zuo, Y.; Liu, J.; Zhang, T.; Tang, P.; Arbiol, J.; Llorca, J.; Cabot, A. NiSn Bimetallic Nanoparticles as Stable Electrocatalysts for Methanol Oxidation Reaction. *Appl. Catal. B Environ.* **2018**, *234*, 10–18.

(55)   Walter, M.; Doswald, S.; Kovalenko, M. V. Inexpensive Colloidal SnSb Nanoalloys as Efficient Anode Materials for Lithium- and Sodium-Ion Batteries. *J. Mater. Chem. A* **2016**, *4* (18), 7053–7059.

(56)   Fjellvåg, H.; Kjekshus, A.; Stomberg, R.; Zingales, R.; Vikholm, I.; Urso, F.; Weidlein, J.; Zingaro, R. A. Structural Properties of Co3Sn2, Ni3Sn2 and Some Ternary Derivatives. *Acta Chem. Scand.* **1986**, *40a*, 23–30.

(57)   Wager, C. D.; Riggs, W. M.; Davis, L. E.; Moulder, J. F.; Muilenderg, G. E. *Handbook of X-Ray Photoelectron Spectroscopy*; Perkin-Elmer Corporation Physical Electronics Division, 1979.

(58)   Liu, Y.; Liu, X.; Feng, Q.; He, D.; Zhang, L.; Lian, C.; Shen, R.; Zhao, G.; Ji, Y.; Wang, D.; et al. Intermetallic Ni $_x M_y$ (M = Ga and Sn) Nanocrystals: A Non-Precious Metal Catalyst for Semi-Hydrogenation of Alkynes. *Adv. Mater.* **2016**, *28* (23), 4747–4754.

(59)   He, M.; Protesescu, L.; Caputo, R.; Krumeich, F.; Kovalenko, M. V. A General Synthesis Strategy for Monodisperse Metallic and Metalloid Nanoparticles (In, Ga, Bi, Sb, Zn, Cu, Sn, and Their Alloys) via in Situ Formed Metal Long-Chain Amides. *Chem. Mater.* **2015**, *27* (2), 635–647.

(60)   Kim, H.-S.; Cook, J. B.; Tolbert, S. H.; Dunn, B. The Development of Pseudocapacitive Properties in Nanosized-MoO2. *J. Electrochem. Soc.* **2015**, *162* (5), A5083–A5090.

(61)   Augustyn, V.; Simon, P.; Dunn, B. Pseudocapacitive Oxide Materials for High-Rate Electrochemical Energy Storage. *Energy Environ. Sci.* **2014**, *7* (5), 1597–1614.

(62)   Xu, X.; Ji, S.; Gu, M.; Liu, J. In Situ Synthesis of MnS Hollow Microspheres on Reduced Graphene Oxide Sheets as High-Capacity and Long-Life Anodes for Li- and Na-Ion Batteries. *ACS Appl. Mater. Interfaces* **2015**, *7* (37), 20957–20964.

(63)   Xu, X.; Liu, J.; Liu, J.; Ouyang, L.; Hu, R.; Wang, H.; Yang, L.; Zhu, M. A General Metal-Organic Framework (MOF)-Derived Selenidation Strategy for In Situ Carbon-Encapsulated Metal Selenides as High-Rate Anodes for Na-Ion Batteries. *Adv. Funct. Mater.* **2018**, *28* (16), 1707573.